

## Structure of Intact AhpF Reveals a Mirrored Thioredoxin-like Active Site and Implies Large Domain Rotations during Catalysis<sup>†,‡</sup>

Zachary A. Wood,<sup>§</sup> Leslie B. Poole,<sup>||</sup> and P. Andrew Karplus<sup>\*,§</sup>

Department of Biochemistry and Biophysics, Oregon State University, Corvallis, Oregon 97331, and  
Department of Biochemistry, Wake Forest University School of Medicine, Winston-Salem, North Carolina 27157

Received December 5, 2000

**ABSTRACT:** AhpF, a homodimer of 57 kDa subunits, is a flavoenzyme which catalyzes the NADH-dependent reduction of redox-active disulfide bonds in the peroxidase AhpC, a member of the recently identified peroxiredoxin class of antioxidant enzymes. The structure of AhpF from *Salmonella typhimurium* at 2.0 Å resolution, determined using multiwavelength anomalous dispersion, shows that the C-terminal portion of AhpF (residues 210–521) is structurally like *Escherichia coli* thioredoxin reductase. In addition, AhpF has an N-terminal domain (residues 1–196) formed from two contiguous thioredoxin folds, but containing just a single redox-active disulfide (Cys129–Cys132). A flexible linker (residues 197–209) connects the domains, consistent with experiments showing that the N-terminal domain acts as an appended substrate, first being reduced by the C-terminal portion of AhpF, and subsequently reducing AhpC. Modeling studies imply that an intrasubunit electron transfer accounts for the reduction of the N-terminal domain in dimeric AhpF. Furthermore, comparing the N-terminal domain with protein disulfide oxidoreductase from *Pyrococcus furiosus*, we describe a new class of protein disulfide oxidoreductases based on a novel mirror-image active site arrangement, with a distinct carboxylate (Glu86) being functionally equivalent to the key acid (Asp26) of *E. coli* thioredoxin. A final fortuitous result is that the N-terminal redox center is reduced and provides a high-resolution view of the thiol–thiolate hydrogen bond that has been predicted to stabilize the attacking thiolate in thioredoxin-like proteins.

The alkyl hydroperoxide reductase system is part of an essential peroxide-inducible response to oxidative stress found in many bacteria (1–3). This system consists of two soluble components, AhpC<sup>1</sup> and AhpF, which together catalyze the NADH-dependent reduction of organic hydroperoxides (or hydrogen peroxide) to their corresponding alcohols and water (Scheme 1) (4, 5).

<sup>†</sup> This work was supported by NIH Grant GM50389. Portions of this work were conducted at the Cornell High Energy Synchrotron Source (CHESS), which is supported by NSF Grant DMR-9311772, using the Macromolecular Diffraction at CHESS (MacCHESS) facility which is supported by NIH Grant RR-01646. Other work was conducted at the Advanced Light Source (ALS), which is supported by the Office of Biological and Environmental Research of the Department of Energy with contributions from Lawrence Berkeley National Laboratory, the National Institute of General Medical Sciences of the National Institutes of Health, and the MCF/ALS participating research team.

<sup>‡</sup> The coordinates and structure factors have been deposited in the Protein Data Bank (PDB) as entry 1HYU.

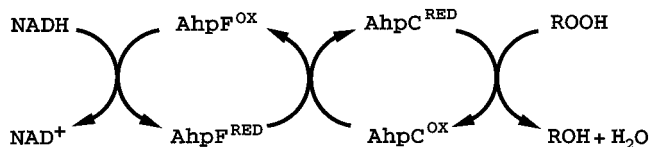
\* To whom correspondence should be addressed: Department of Biochemistry and Biophysics, Oregon State University, Corvallis, Oregon 97333. E-mail: karplusp@ucs.orst.edu. Phone: (541) 737-3200. Fax: (541) 737-0481.

<sup>§</sup> Oregon State University.

<sup>||</sup> Wake Forest University School of Medicine.

<sup>1</sup> Abbreviations: AhpF, alkyl hydroperoxide reductase flavoprotein or NADH:peroxiredoxin oxidoreductase; AhpC, alkyl hydroperoxide reductase peroxidase component (member of the peroxiredoxin family); NTD, N-terminal domain of AhpF; TrxR, thioredoxin reductase; Trx, thioredoxin; PDO, protein disulfide oxidoreductase; MAD, multiwavelength anomalous dispersion; Se-Met, selenomethionine; FPLC, fast protein liquid chromatography; GDX, glutaredoxin.

Scheme 1



AhpC, a 210 kDa homodecamer, is a member of the recently described peroxiredoxin family (6, 7). AhpF, a homodimer of 57 kDa subunits, is an FAD-dependent NADH: protein-disulfide reductase which reduces redox-active disulfides in AhpC during catalytic turnover (8, 9).

AhpF is comprised of three domains: an N-terminal redox-active disulfide-containing domain (NTD), an FAD binding domain (FAD), and an NADH binding redox-active disulfide-containing domain (NADH/SS) (8, 10). Limited proteolysis separates AhpF into two soluble fragments, both of which are required for the NADH-driven reduction of AhpC (8, 11). The larger of the two fragments (residues 203–521) contains the FAD and NADH/SS domains, and retains NADH-dependent transhydrogenase and oxidase activities, but is not able to reduce AhpC (8). This fragment is homologous (34% identical sequence) to *Escherichia coli* thioredoxin reductase (TrxR), including the conservation of a redox-active disulfide involving Cys345 and Cys348 in the NADH/SS domain (7, 8, 10). The smaller proteolytic fragment (residues 1–202) contains the NTD and has a second redox-active disulfide between Cys129 and Cys132

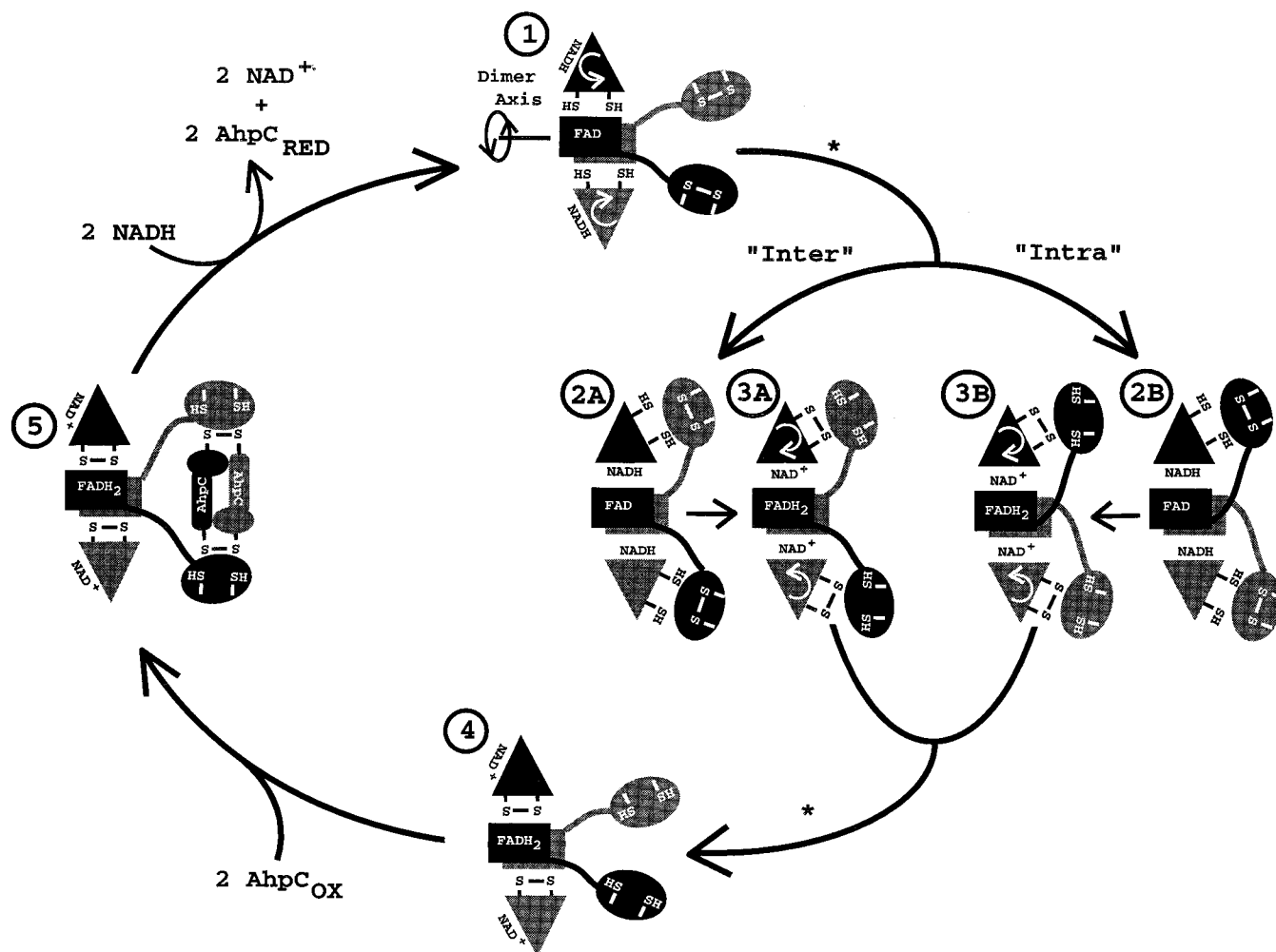


FIGURE 1: Proposed catalytic cycle of AhpF. AhpF is depicted as a "head-to-tail" homodimer, oriented with its dimer axis in the plane of the page. Individual subunits are colored gray or black. The NADH/SS domain (triangle) is shown with either  $\text{NAD}^+$  or  $\text{NADH}$  bound, and its redox center (Cys345–Cys348) is shown in either the oxidized (S–S) or reduced  $[(\text{SH})_2]$  form. White circular arrows denote domain rotations. The FAD domain (rectangle) has either oxidized (FAD) or reduced ( $\text{FADH}_2$ ) flavin. The NTD's (ovals) redox center (Cys129–Cys132) is depicted in either the oxidized (S–S) or reduced  $[(\text{SH})_2]$  form. Both possible pathways for NTD reduction, intermolecular (via **2A**  $\rightarrow$  **3A**) and intramolecular (via **2B**  $\rightarrow$  **3B**), are illustrated. Asterisks in the paths indicate conformational changes. AhpC is represented as  $\text{AhpC}_{\text{OX}}$  (oxidized) or  $\text{AhpC}_{\text{RED}}$  (reduced). For simplification, reactions and conformational changes in both subunits of the dimer or with AhpC are depicted as synchronous events. This figure has been adapted from Poole et al. (9).

(7, 8, 11). The NTD is directly responsible for the ability of AhpF to reduce redox-active disulfides in AhpC (8, 11). The NTD is predicted to be homologous to the thioredoxin-like (Trx-like) protein disulfide oxidoreductase from *Pyrococcus furiosus* (PpPDO) (23% identical sequence) (11). The crystal structure of PpPDO reveals that it consists of two fused thioredoxin folds (12). Both redox-active disulfide centers in AhpF are formed by cysteinyl residues within the CXXC structural motif common to both thioredoxin (Trx) and TrxR.

The proposed mechanism of AhpF is analogous to that deduced for the Trx/TrxR system (9, 13, 14). Briefly, the FAD and NADH/SS domains of AhpF are joined by two extended  $\beta$ -strands, forming a flexible "neck", with the NADH binding site and the Cys345–Cys348 redox center some distance from one another in the NADH/SS domain (11). During catalysis, the entire NADH/SS domain rotates, bringing a bound  $\text{NADH}$  to the *re* face of the isoalloxazine ring for oxidation and the dithiol to the surface where it can reduce the disulfide in the NTD (Figure 1). A second rotation brings the newly formed disulfide back to the *re* face of the

isoalloxazine ring where it is reduced, and the  $\text{NAD}^+$  to the surface for exchange, thereby completing the transfer of electrons from  $\text{NADH}$  to the NTD. In the first step, the NTD acts as an "appended" substrate for the TrxR-like portion of AhpF, and then the reduced NTD acts as a protein disulfide reductase for AhpC (9, 11, 15, 16). Mechanisms for the dithiol–disulfide exchange in AhpF are as yet poorly understood. In solution, AhpF forms a head-to-tail homodimer, presenting the possibility that electron transfer from the NADH/SS domain to the NTD redox-active disulfide could occur via two possible pathways in the homodimer: intrasubunit or intersubunit (Figure 1, steps 2 and 3) (9).

Here we report the 2.0 Å resolution crystal structure of intact AhpF from *Salmonella typhimurium* determined using multiwavelength anomalous dispersion (MAD) phasing, and present strong evidence supporting the intrasubunit pathway as the path for NTD reduction. In addition, we identify a new family of Trx-like protein disulfide reductases (peroxiredoxin disulfide reductases) based on the novel active site architecture of the NTD. Finally, the structure fortuitously provides us with a high-resolution view of a thiol–thiolate

hydrogen bond, predicted to play a central role in the mechanism of Trx-like disulfide reductases.

## EXPERIMENTAL PROCEDURES

**Purification of AhpF and Se-Met AhpF.** AhpF was expressed and purified essentially as described previously (4). For selenomethionine (Se-Met) incorporation, the same plasmid (pAF1) was transformed into the methionine auxotroph B834(DE3) (Novagen, Inc., Madison, WI). Expression of Se-met AhpF followed methods used previously by Ramakrishnan et al. (17). The medium consisted of 2× M9 salts supplemented with 0.4% glucose, amino acids (excluding methionine) at 40 μg/mL each, seleno-L-methionine from Sigma at 40 μg/mL, and four vitamins (riboflavin, niacinamide, pyridoxine monohydrochloride, and thiamine) at 1 μg/mL each. Chloramphenicol at 25 μg/mL was included.

Two cultures (750 mL each) in the medium described above were grown overnight (~15 h) at 37 °C. IPTG was added when  $A_{600}$  equaled 1.5, and incubation continued for an additional 6.5 h. Purification of Se-Met AhpF was as previously described (4), with the following modifications. Following the streptomycin sulfate treatment, the supernatant was subjected to a 30 to 80% ammonium sulfate cut, and after the resuspended pellet was dialyzed against 5 mM potassium phosphate (two changes), it was loaded onto a 25 mL Q-Sepharose FPLC column (same buffer), and then eluted with a potassium phosphate gradient (5 to 65 mM). The final Affi-Gel Blue column (4) yielded 9 mg of Se-Met AhpF.

**Crystallization and Microseeding of AhpF.** Using hanging drops and the sparse matrix strategy (18), a crystallization lead that could be optimized was obtained. In initial optimization trials, it was noted that chloride had a positive effect on crystallization, leading to single cube-like crystals instead of crystalline material resembling bundles of twigs. Single crystals were grown at 4 °C using 1.7 M ammonium sulfate, 1.0 M lithium chloride, and 0.1 M citrate (pH 5.6) as a reservoir, and 2 μL of a 10 mg/mL stock solution of AhpF mixed with 2 μL of the reservoir for the drop. Crystals grew rarely and took 12–24 weeks to appear, reaching a maximum size of 0.2 mm × 0.2 mm × 0.2 mm. For data collection, crystals were dipped (~30 s) into a cryoprotectant solution containing 20% (w/v) glycerol in addition to the reservoir solution above, and then either flash-cooled in a –170 °C nitrogen stream or by plunging the sample into liquid nitrogen (19).

The slow and infrequent crystallization led us to believe that nucleation was the limiting step, so we developed a microseeding strategy as follows; several small crystals were pooled into a depression slide containing 100 μL of the reservoir solution, and crushed using the bevelled end of a 22 gauge hypodermic needle. The resulting seed stock solution was mixed and used to make serial 10-fold dilutions from which 0.5 μL was added to a pre-equilibrated (1 week) drop of AhpF (same conditions as described above). Crystals grew reproducibly in 1–3 weeks. Se-Met crystals grown this way were small (0.05 mm × 0.05 mm × 0.03 mm), but nonetheless diffracted to 2.5 Å resolution at the Advanced Light Source (ALS).

**X-ray Diffraction Data Collection.** Crystal data are reported in Table 1. A native data set to 2.0 Å resolution was

Table 1: Data Collection Statistics

Crystal Data				
space group	$P2_12_12$			
unit cell	$a = 102.2 \text{ \AA}$ , $b = 139.2 \text{ \AA}$ , $c = 39.1 \text{ \AA}$			
solvent content	46%			
no. of protein molecules <sup>a</sup>	1 (521 residues)			
no. of FAD molecules <sup>a</sup>	1			
no. of Se-methionines <sup>a</sup>	9			
Data Collection Statistics				
	native <sup>b</sup>	edge <sup>c</sup>	peak <sup>c</sup>	remote <sup>c</sup>
wavelength (Å)	0.92300	0.97980	0.97961	0.96482
resolution (Å)	2.0	2.5	2.5	2.5
no. of total observations	106083	43295	42201	41723
no. of unique reflections	36494	17925	17825	17774
completeness	95.4 (98.6) <sup>d</sup>	90.9 (87.7)	90.2 (84.7)	89.8 (85.3)
$I/\sigma$	11.0 (5.0)	9.8 (3.6)	9.4 (3.4)	8.4 (2.7)
$R_{\text{meas}}^e$	10.6 (30.5)	11.0 (36.2)	11.1 (41.3)	15.0 (62.2)

<sup>a</sup> Unique contents of the unit cell. <sup>b</sup> Data collected at CHESS. <sup>c</sup> Data collected at ALS. <sup>d</sup> Numbers in parentheses represent data for the highest-resolution shell. <sup>e</sup>  $R_{\text{meas}}$  is the multiplicity-weighted merging  $R$ -factor of Diederichs and Karplus (22).

collected at beamline F1 of the Cornell High Energy Synchrotron Source (CHESS), using a single frozen crystal of AhpF. Using an ADSC Quantum-4 mosaic CCD-based X-ray detector (Area Detector System Corp.), 184° of data were collected (60 s per 0.8° frame). A three-wavelength MAD data set was collected from a single crystal of Se-Met AhpF at beamline 5.0.2 of the Advanced Light Source (ALS) using an ADSC Quantum-4 X-ray detector. A fluorescence scan determined the two optimum wavelengths to minimize the  $f'$  (edge) and to maximize the  $f''$  (peak) contributions. A third wavelength was chosen to be 200 eV higher than the peak (remote) to maximize the dispersive differences ( $\Delta f'$ ) between wavelengths. On the basis of the crystal orientation, the optimal strategy for a >90% complete, 2.5 Å resolution data set required 60° of data. Using the inverse beam method on every 10° wedge of data for the Bijoets (30 s per 1° frame), three complete data sets were collected: first the edge, then the peak, and finally the remote.

**Data Processing.** All frames were corrected for background, spatial distortion and nonuniformity. Native data (Table 1) were processed using the CCP4 programs MOSFLM and SCALA (20). The MAD data sets (Table 1) were processed using the HKL suite of programs (21). The program NovelR calculated the multiplicity-weighted merging  $R$ -factors (22).

**Locating the Se Sites and MAD Phasing.** Estimates of  $f'$  and  $f''$  for each wavelength were obtained directly from the fluorescence scan using the program KK (K. Henderson, personal communication). Using the CNS suite of programs, the three MAD data sets were scaled together and a merged Patterson map (combining anomalous Patterson maps for each wavelength and a dispersive Patterson map between the edge and remote) was calculated using data between 15 and 4 Å resolution (23). Our initial search for Se sites using the automated Patterson map searching routine in CNS failed. Given the weaker statistics for the remote wavelength (Table 1), we repeated the calculations using only the edge and peak

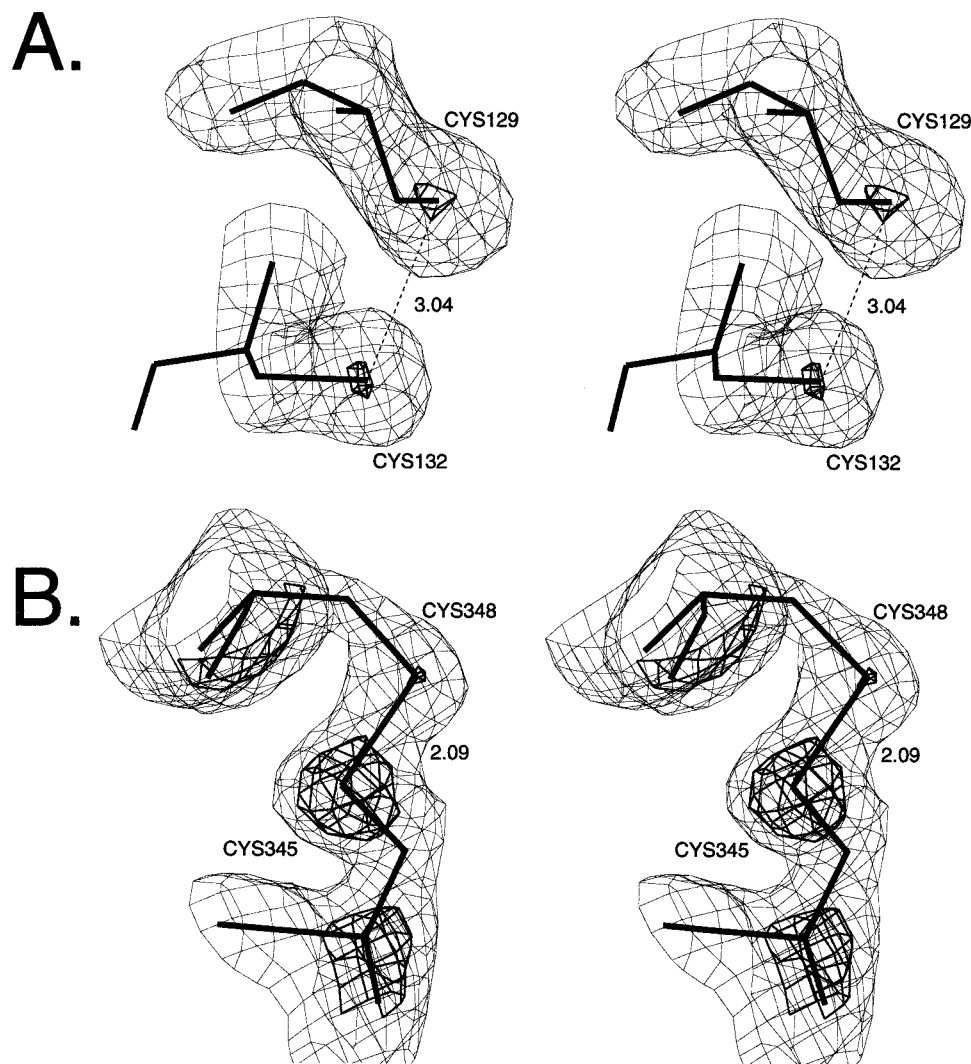


FIGURE 2: Electron density for redox-active centers. Stereoviews show the  $2F_o - F_c$  electron density contoured at  $1\sigma$  (thin lines) and either  $3.5\sigma$  or  $3.0\sigma$  (thick lines) in panels A and B, respectively. (A) The dithiol form of the NTD redox center (Cys129–Cys132). No significant difference ( $F_o - F_c$ ) density is observed in the vicinity of the dithiol center, and the  $2F_o - F_c$  density is well-formed, with no suggestion of a mixture of disulfide and dithiol states. The  $B$ -factors for Cys129 and Cys132  $S_\gamma$  are 49 and 44  $\text{\AA}^2$ , respectively, comparable to the values of 38 and 34  $\text{\AA}^2$  for their respective  $C_\alpha$  atoms. Sulfur–sulfur distances (in angstroms) are shown with dashed lines. (B) The disulfide form of the NADH/SS redox center (Cys345–Cys348). The  $B$ -factors for Cys345 and Cys348  $S_\gamma$  atoms refined to 54 and 65  $\text{\AA}^2$ , respectively, and 37 and 40  $\text{\AA}^2$  for their respective  $C_\alpha$  atoms, illustrating a significant degree of disorder in this disulfide.

wavelengths. This approach yielded a clear solution for six sites that were refined and used for phasing to 3  $\text{\AA}$  resolution. Difference maps calculated with these phases revealed positions for two additional Se atoms, and phases to 3  $\text{\AA}$  resolution (figure of merit of 0.55) were then calculated using all three wavelengths.

**Model Building and Refinement.** All model building was carried out using the program CHAIN (24). Electron density modification and model refinement were performed using CNS. The 3  $\text{\AA}$  MAD electron density map was subjected to 40 cycles of solvent flipping (25) with 45% solvent content. The resulting map revealed helices and sheets, and despite poor connectivity guided the building of a partial model for the FAD and NADH/SS domains based on *E. coli* TrxR (PDB entry 1TDF). Ten percent of the data were set aside for cross-validation. For initial refinements, torsion angle dynamics were used with the maximum likelihood target restrained by experimental phases, followed by phase combination and solvent flipping. After extension of the resolution to 2.5  $\text{\AA}$ , the model for the TrxR-like portion of AhpF was

completed. Examination of the electron density for the NTD revealed eight  $\beta$ -strands in a sheet and five  $\alpha$ -helices. A poly-Ala model based on PfpDO was manually docked into the density, and secondary structure elements were adjusted by fitting each as a separate unit. Assigning side chains based on Se atom positions revealed one of the Se sites to be the N-terminal methionine, which we had assumed was absent, for a total of nine Se atoms in the asymmetric unit. The Se atom missing from the MAD model, Met169, was located on the surface and was mobile (final  $B$ -factor for  $S_\delta$  is 86  $\text{\AA}^2$ ). With the model complete, we switched to the native data set while preserving the cross-validation test set. The resolution was extended to 2.0  $\text{\AA}$ , and the electron density for the NTD redox center indicated it was not a disulfide (Figure 2). Difference maps ( $F_o - F_c$ ) produced a large negative ( $\sim 6\sigma$ ) and two positive ( $3\text{--}4\sigma$ ) peaks indicating that the sulfurs needed to move apart. The  $2F_o - F_c$  maps showed peak densities for the sulfur atoms  $\sim 3$   $\text{\AA}$  apart. To remove bias, we refined Cys129 and Cys132 as alanines and the resulting density confirmed there was no disulfide bond.

Table 2: Crystallographic Refinement Statistics

resolution range (Å)	50.0–2.0
amplitude cutoff	none
no. of amino acid residues	521
no. of sulfates	2
no. of chlorides	1
no. of waters	352
no. of total non-H atoms	4283
average <i>B</i> -factor (Å <sup>2</sup> )	
protein	33
NTD	34
FAD domain	25
NADH/SS domain	42
solvent	46
<i>R</i> -factor	0.182
free <i>R</i> -factor (10% of the data)	0.235
stereochemical ideality	
bond length rmsd (Å)	0.016
bond angle rmsd (deg)	1.7
$\phi$ , $\psi$ most favored (%)	89.6
$\phi$ , $\psi$ additional allowed (%)	10.2
$\phi$ , $\psi$ generously allowed (%)	0.2

Further refinement with individual *B*-factor refinement reduced the *R*-factor to 23.0% (*R*-free = 29.1%).

At this stage, we abandoned torsion angle dynamics in favor of Powell minimization. Waters were added both manually and using the Water-Pick utility in CNS with the following criteria: (1) a minimum  $3\sigma$  peak in  $F_o - F_c$  maps and (2) a minimum distance of 2.6 Å and a maximum distance of 3.5 Å to donors or acceptors. Two sulfate ions were identified on the basis of tetrahedral density and hydrogen bonding environment. Sulfate 800 is hydrogen bonded to the guanidinium groups of Arg430 and Arg432 in the NADH/SS domain, and sulfate 801 makes hydrogen bonds to the N $\delta$  of His438, to both the hydroxyl and peptide nitrogen of Ser439, and to the amino group of Lys179 of a symmetry-related molecule. Finally, a well-ordered chloride ion was identified at the *re* face of the isoalloxazine ring based on electron density strength, hydrogen bonding distances, knowledge of the components of the crystallization buffer, and reasonable refined *B*-factors with regard to the surrounding ligands. The final model statistics are reported in Table 2.

**Structure and Sequence Analysis.** Sequence alignments were determined using PIMA (26, 27) and SEQUOIA (C. Bruns, personal communication). HOMOLOGCORE (P. A. Karplus) was used to create structural overlays for comparisons. DOMOV (G. Lu, personal communication) was used to determine relative changes in domain orientations between homologous structures. The DALI (28) search and structure comparison algorithm was used to find and analyze structurally similar homologues. Structural figures were generated using MOLSCRIPT (29).

**Modeling the Alternate Conformation of AhpF.** Using the recently determined *E. coli* TrxR–Trx mixed disulfide with the NADHP/SS domain in the alternate conformation (PDB entry 1F6M) (14), we modeled a hypothetical alternate conformation for AhpF. We separated the AhpF structure into three pieces: the NTD and linker domains (residues 1–209), the FAD domain (residues 210–327 and 450–521), and the NADH/SS domain (residues 328–449). We overlaid the FAD and NADH/SS domains of AhpF with the corresponding domains of 1F6M. Only a minor adjustment of the connecting  $\beta$ -strands was required. Finally, the NTD was

overlaid with the covalently bound Trx in the *E. coli* TrxR structure based on C $\alpha$  atoms. The NTD was reconnected to the FAD domain by adjusting the linker (residues 195–209) in a manner that would preserve reasonable geometry.

## RESULTS

**Overall Structure of AhpF.** The crystal structure of AhpF reveals one monomer in the asymmetric unit, with the complete AhpF homodimer generated by the crystallographic 2-fold axis (Figure 3). All 521 residues of AhpF are modeled, with just one loop (residues 198–201) having high temperature factors (>70 Å<sup>2</sup> for C $\alpha$  atoms), but the main chain path is clear. The AhpF structure is divided into four distinct regions: the NTD (residues 1–196), a linker segment (residues 197–209) containing the weakly ordered loop, the FAD domain (residues 210–327 and 450–521), and the NADH/SS domain (residues 328–449). The NADH/SS domain is, as a unit, less ordered than the other domains (Table 2). The C-terminal portion of AhpF (residues 210–521) is homologous to *E. coli* TrxR, and will be referred to as the TrxR-like portion of AhpF. The NADH/SS domain is oriented with its NAD binding site exposed, and its redox-active disulfide near the flavin. The redox center (Cys345–Cys348) in the NADH/SS domain is 33 Å from the redox center (Cys129–Cys132) in the NTD.

**TrxR-like Portion of AhpF.** The NADH/SS and FAD domains of AhpF each consist of a central five-stranded  $\beta$ -sheet, flanked on one side by a smaller three-stranded  $\beta$ -sheet, and on the other side by  $\alpha$ -helices (three in the FAD domain and two in the NADH/SS domain). The structure is very similar to that of *E. coli* TrxR [rmsd = 1.4 Å for either 175 C $\alpha$  atoms in FAD domains or 124 C $\alpha$  atoms in the NAD(P)H/SS domains when the domains are separately overlaid]. Relative to the FAD domain overlay, the NAD(P)H/SS domain overlay differs by a 16.2° rotation accompanied by a translation of 1.5 Å, and the dimer interface is conserved between the two structures. Many minor differences exist between the structures, including nine insertions and/or deletions that occur in loops (Figure 4B). Two noteworthy structural differences exist in the pyridine nucleotide binding site and the active site containing the redox-active disulfide (Cys345–Cys348).

First, AhpF differs from *E. coli* TrxR in its specificity for pyridine nucleotides. Lacking a structure of AhpF with NADH (or NAD<sup>+</sup>) bound, we examined an overlay with the TrxR structure with NADP<sup>+</sup> bound (PDB entry 1TDF). In TrxR, NADP<sup>+</sup> binds to the  $\beta\alpha\beta$  unit ( $\beta_9\alpha_5\beta_{10}$  in Figure 4B) containing the conserved structural motif Gly-X-Gly-X-X-Ala common to NADP<sup>+</sup> binding enzymes (30). In addition, His175 and Arg176 in *E. coli* TrxR make strong, favorable interactions with the 2'-phosphate of the adenine base (13). In AhpF, as well as other NADH binding enzymes (31), the Ala in the conserved structural motif of the  $\beta\alpha\beta$  unit is replaced with a Gly. Also, His175 and Arg176 of *E. coli* TrxR are replaced with Glu385 and Phe386, respectively, creating a highly unfavorable environment for a negatively charged phosphate. We propose that, as was seen in protein engineering studies with glutathione reductase (32), these three residues are the primary specificity determinants in AhpF.

The second difference between AhpF and TrxR involves the placement and geometry of the redox-active disulfide.

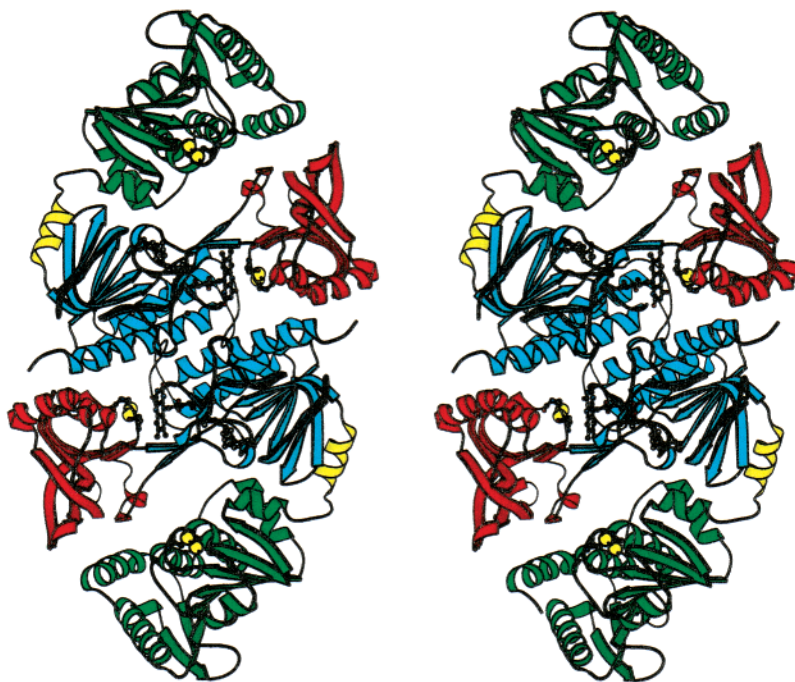


FIGURE 3: Stereoview of the AhpF dimer colored by domain. The second subunit was generated by the crystallographic 2-fold. The NTD (green), shown with its redox-active dithiol (Cys129–Cys132), is connected by the flexible linker (yellow) to the FAD domain (blue), and the NADH/SS domain (red) is depicted with its redox-active disulfide (Cys345–Cys348). The bound flavin cofactor in the FAD domain is also shown. This figure was generated using MOLSCRIPT (29).

In *E. coli* TrxR, the CXXC motif sits above the flavin and forms a short (four-residue)  $\alpha$ -helix with the redox-active disulfide adopting a right-handed hook conformation (Figure 5A). In AhpF, this position is occupied by a bound chloride and the CXXC is shifted away, adopting a nonhelical conformation that makes several favorable interactions with the chloride (Figure 5B). The displaced CXXC motif does not form a right-handed hook, but instead adopts a left-handed spiral conformation. Though the disulfide torsion angle ( $-108^\circ$ ) is within the range commonly observed for disulfides, the disulfide itself is disordered and strained as evidenced by high *B*-factors (Figure 2B) and poor geometry. Both Cys345 and Cys348 occupy the infrequently observed (due to steric hindrance) *gauche*<sup>+</sup> rotomer (33), with the Cys348 S<sub>γ</sub> atom in van der Waals contact (3.4 Å) with the carboxylate of the catalytically important (34) Asp349 (Figure 5B).

**NTD Linker.** The linker segment (residues 197–209) is known to be flexible in solution because limited proteolysis readily cleaves after Arg202 (8, 11). Consistent with this, the sequence has many charged residues (6 of 13), two polar (Thr197 and Asn208) residues, four small aliphatics (Ala and Gly), and only one bulky hydrophobic (Leu207) residue. The linker adopts a loop–helix conformation in this crystal structure with the loop (residues 197–200) being very poorly ordered and the helix (residues 201–209) having high *B*-factors for its first three residues ( $>50 \text{ \AA}^2$  for main chain atoms). The helix interacts weakly with the FAD domain, making only one hydrogen bond (Asn208 O<sub>δ</sub> with Val312 N) and burying just Leu207 against Ile285 and Leu313.

**NTD.** As predicted (11), the NTD consists of two “fused” thioredoxin folds, forming a contiguous eight-stranded  $\beta$ -sheet sandwiched between six  $\alpha$ -helices on one side and one  $\alpha$ -helix and three extended loops on the other (Figure 6A). Surprisingly, the NTD redox center (Cys129–Cys132)

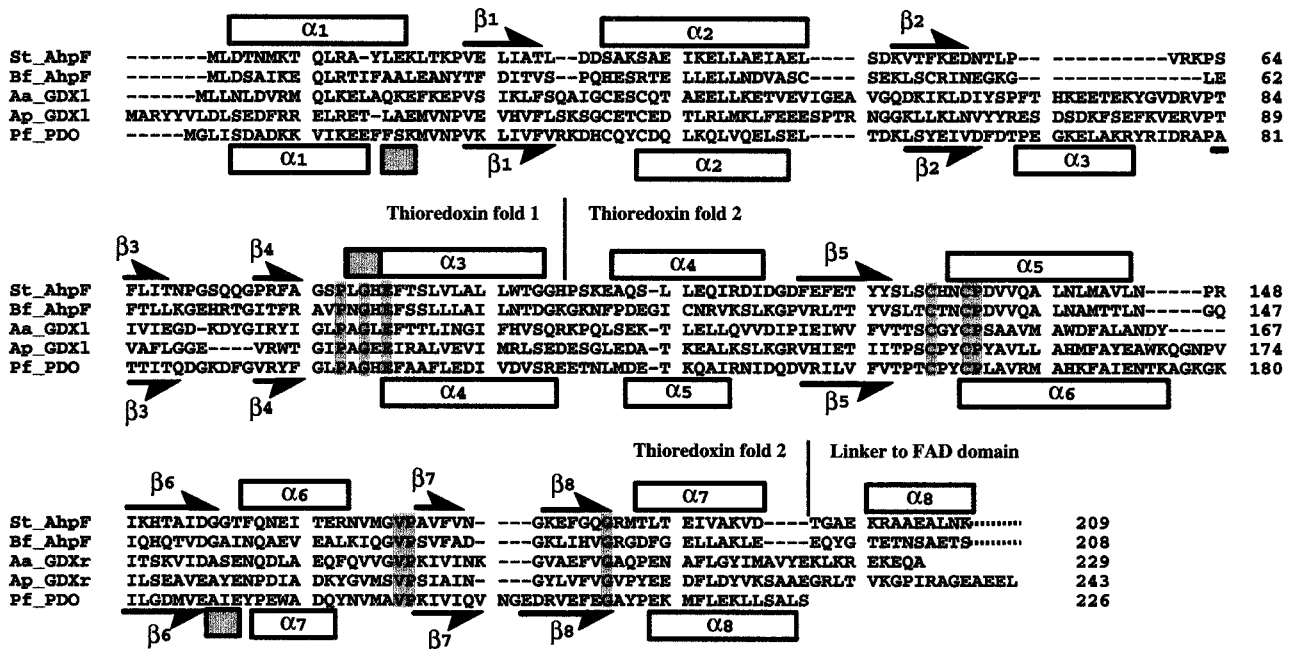
which is in the C-terminal thioredoxin fold is in its reduced (dithiol) form (Figure 2A), although no precautions had been taken to preserve that state. The sulfur–sulfur distance between the cysteines is  $\sim 3.04 \text{ \AA}$  (see the Discussion).

A structural overlay of the NTD with *Pf*PDO shows them to be very similar (Figures 4A and 6B). In addition to the overall similarities in fold, both *Pf*PDO and the NTD contain two structurally conserved *cis*-prolines: *cis*-Pro63 at the beginning of  $\beta$ -strand 3 and *cis*-Pro172 at the beginning of  $\beta$ -strand 7. Two notable differences are the deletion of *Pf*PDO $\alpha$ 3 in the NTD and the presence in *Pf*PDO of two disulfides, one in each thioredoxin fold.

The N-terminal disulfide that is fully buried in *Pf*PDO (12) is replaced with an extension of an  $\alpha$ -helix ( $\alpha$ 2) in the NTD. The C-terminal redox-active disulfide is common to both structures, and its conformation is highly similar.

BLAST (35) searches with the NTD and *Pf*PDO identified five similar proteins of unknown function described as glutaredoxin-like (GDX-like). A sequence alignment of the NTDs from 14 available AhpF sequences, *Pf*PDO, and the five GDX-like proteins reveals the striking conservation of nine residues (Figure 4A). Interestingly, all nine of the absolutely conserved residues are in the immediate vicinity of the C-terminal active site (Figure 6C). Cys129 is solvent-exposed, while Cys132 is buried in a mostly hydrophobic pocket made up of conserved residues, Val171 and *cis*-Pro172. The conserved Gly184 ( $\phi = 84^\circ$ ,  $\psi = -176^\circ$ ) is on the distal side of Pro172, at the end of  $\beta$ -strand 8. Below the CXXC is a conserved buried acid, Glu86, surrounded by hydrophobic residues Pro133 (conserved), Tyr125, and Val136. Glu86 is hydrogen bonded only to the Ser89 hydroxyl (2.6 Å) and a single water molecule, W98 (2.8 Å). Water molecule W98 also makes hydrogen bonds to Ser126 O (2.6 Å) and to Cys129 O (2.8 Å). Conserved residues Pro82 and Gly84 make up the loop containing Glu86, and

## A.



## B.

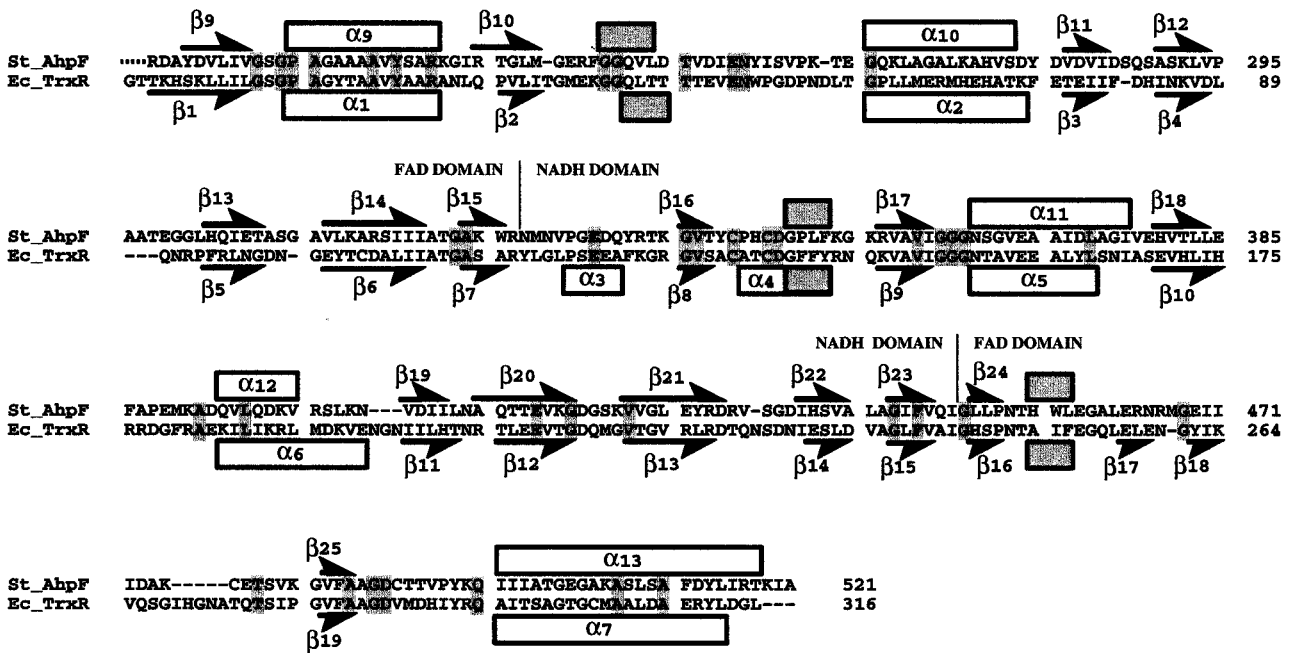


FIGURE 4: Structure-based sequence alignments of AhpF and its homologues. Helices are represented by rectangles (white for  $\alpha$ -helices and gray for  $3_{10}$ -helices), and  $\beta$ -strands are represented by arrows. Absolutely conserved residues in the alignments are shaded. (A) Alignment of NTDs and NTD-related homologues (GDXI for glutaredoxin-like and PDO for protein disulfide oxidoreductase). The alignment was constructed using 16 sequences, but for simplicity, only the five most divergent are shown, with levels of cross sequence identity ranging from 16 to 38% [*S. typhimurium* (*St\_AhpF*), *Bacteriodes fragilis* (*Bf\_AhpF*), *Aquifex aeolicus* (*Aa\_GDXI*), *Aeropyrum pernix* (*Ap\_GDXI*), and *Pyrococcus furiosus* (*Pf\_PDO*)]. Only secondary structure elements for *St\_AhpF* (top line) and *Pf\_PDO* (bottom line) are available for guiding the alignment. Vertical lines delineate the first thioredoxin fold from the second and the second from the flexible linker. Dots at the end of the *St\_AhpF* and *Bf\_AhpF* sequences indicate that those sequences are continued. Species (GenBank accession numbers) for the 16 sequences that were used: *A. pernix* (A72669), *Aq. aeolicus* (E70340), *Pyrococcus abyssi* (F75204), *Pyrococcus horikoshii* (H71239), *Thermatoga maritima* (G72322), *Pseudomonas aeruginosa* (AAG03530), *Amphibacillus xylanus* (BAA33809), *B. fragilis* (AAD52148), *Bacillus alcalophilus* (JX0166), *Bacillus subtilis* (BAA11269), *E. coli* (P35340), *Pseudomonas putida* (BAA31469), *Staphylococcus aureus* (AAB51152), *Streptococcus mutans* (BAA25696), *S. typhimurium* (114049), *Thermus aquaticus* (AAF82119), *Xanthomonas campestris* (AAC45426), *Xylella fastidiosa* (AAF84340), and *P. furiosus* (4699595). (B) Alignment of the C-terminal portion of AhpFs and TrxRs using 19 available sequences. Only the sequences of *S. typhimurium* (*St\_AhpF*) and *E. coli* (*Ec\_TrxR*) are shown with their respective secondary structures indicated above or below the sequences. Vertical lines delineate the NADH/SS domain from the two parts of the FAD domain. Dots at the beginning of the *St\_AhpF* sequence indicate that it is continued from panel A.

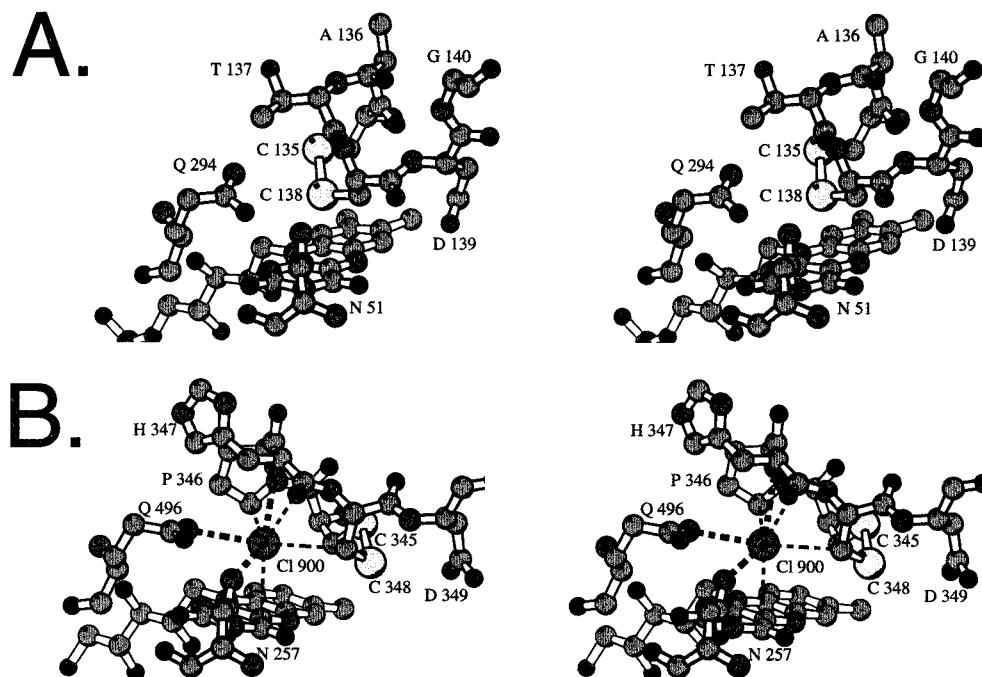


FIGURE 5: Disruption of the NADH/SS active site by chloride binding. (A) Stereoview of the *E. coli* TrxR active site (PDB entry 1TDE), with the CXXC motif in a short  $\alpha$ -helix, and the disulfide in a right-handed hook conformation, placing the  $S_{\gamma}$  atom of Cys138 3.1 Å from  $C_{4a}$  above the *re* face of the isoalloxazine ring. (B) Binding of chloride in the TrxR-like active site of AhpF. The chloride is depicted as a sphere with hydrogen bonding and other close interactions indicated with dashed lines: hydrogen bonds to His347 N (3.2 Å), Gln496  $N_{\epsilon}$  (3.2 Å), and Asn257  $N_{\delta}$  (3.7 Å) and close packing interactions for FAD  $C_4$  (3.5 Å), His347 C (3.6 Å), Cys348  $C_{\beta}$  (3.7 Å), and Pro346  $C_{\delta}$  (3.8 Å). The CXXC motif is nonhelical, and the disulfide is in a left-handed spiral conformation. The  $\chi_1$  and  $\psi$  torsion angles of Cys345 (78° and 132°, respectively) bring the  $S_{\gamma}$  and carbonyl oxygen within 3.1 Å of one another. Cys348's  $\chi_1$  torsion angle of 95° brings the  $S_{\gamma}$  in close contact with its own carbonyl carbon (3.0 Å) and the carboxylate of Asp349 (3.4 Å). The chloride is in the approximate position that would be occupied by Cys348  $S_{\gamma}$  if the disulfide were in a right-handed hook conformation, as in TrxR (panel A). The shifted disulfide in AhpF is not in a favorable position for reduction by the flavin. This figure was generated using MOLSCRIPT (29).

they may aid in its proper positioning. Finally, Ser126 (conserved as a serine or threonine) is involved in a type I turn immediately preceding the active site, with Ser126  $O_{\gamma}$  and Ser126 O hydrogen bonding to Cys129 N (3.0 and 3.1 Å, respectively). In oxidized *Pf* PDO, the equivalent turn is a nonclassical turn, in which the  $\psi$  torsion angle of the residue preceding the cystine is rotated, so that the backbone amide is not oriented for hydrogen bonding.

Comparing the second half of the NTD to *E. coli* Trx reveals that the major structural distinction with regard to the fold is with the first  $\alpha$ -helix, which packs on opposite faces of the central  $\beta$ -sheet (Figure 7A). Despite a low degree of sequence identity (16%), the active site dithiols and disulfides are very similar in the structural overlay. In Trxs, Asp26 is absolutely conserved and catalytically crucial (36–39). Although there is no corresponding acid conserved in sequence in the NTD, Glu86 appears to be a functionally equivalent residue; it is also a buried acid positioned beneath the redox-active disulfide and likewise hydrogen bonded to a nearby water molecule that could act to shuttle protons to the solvent. In the overlay, the active site sulfur atoms of both NTD and Trx, as well as the carboxylates of Asp26 and Glu86, lie in the same plane, although the acids are not superimposable (Figure 7B).

**A Modeled Alternate Conformation of AhpF.** On the basis of the homology between the C-terminal portion of AhpF and *E. coli* TrxR, as well as the NTD compared to *E. coli* Trx, we expect that NTD reduction will be very similar to thioredoxin reduction by TrxR. In support of this view, protein engineering to attach the NTD and part of the linker

(residues 1–207) to the N-terminus of *E. coli* TrxR produced a chimeric protein that could reduce AhpC nearly as efficiently as native AhpF (15). Recently, the crystal structure of *E. coli* TrxR containing a mixed disulfide with Trx has been reported (14). On the basis of this crystal structure (PDB entry 1F6M), we are able to model a plausible conformation for reduction of the NTD in AhpF (see Materials and Methods) (Figure 8). Compared to our crystal structure, this conformation has the NADH/SS domain rotated 57°, and the NTD rotated 100° and shifted by 8 Å. Remarkably, we observe that there are no major steric clashes that would prevent such a rotated conformation in AhpF (some side chains would require minor adjustments). The modeled interfacial active site closely matches that of the *E. coli* TrxR–Trx mixed disulfide, and verifies Cys129 as the target of attack by the thiolate of Cys348 in the NADH/SS domain. In support of the proposed intramolecular pathway for NTD reduction (Figure 1, steps 2B  $\rightarrow$  3B), the NTD easily connects to its own AhpF subunit in the structure by unraveling the first turn of the helical portion of the linker. However, the 70 Å distance from the NTD C-terminus to the N-terminus of the FAD domain in the other subunit means modeling the intermolecular pathway is not possible on the basis of this analogy.

## DISCUSSION

**Overall Structural Observations of AhpF.** The crystal structure of AhpF reveals one subunit of the homodimer, with its dimer axis coincident with the crystallographic 2-fold. AhpF is composed of three distinct domains, with

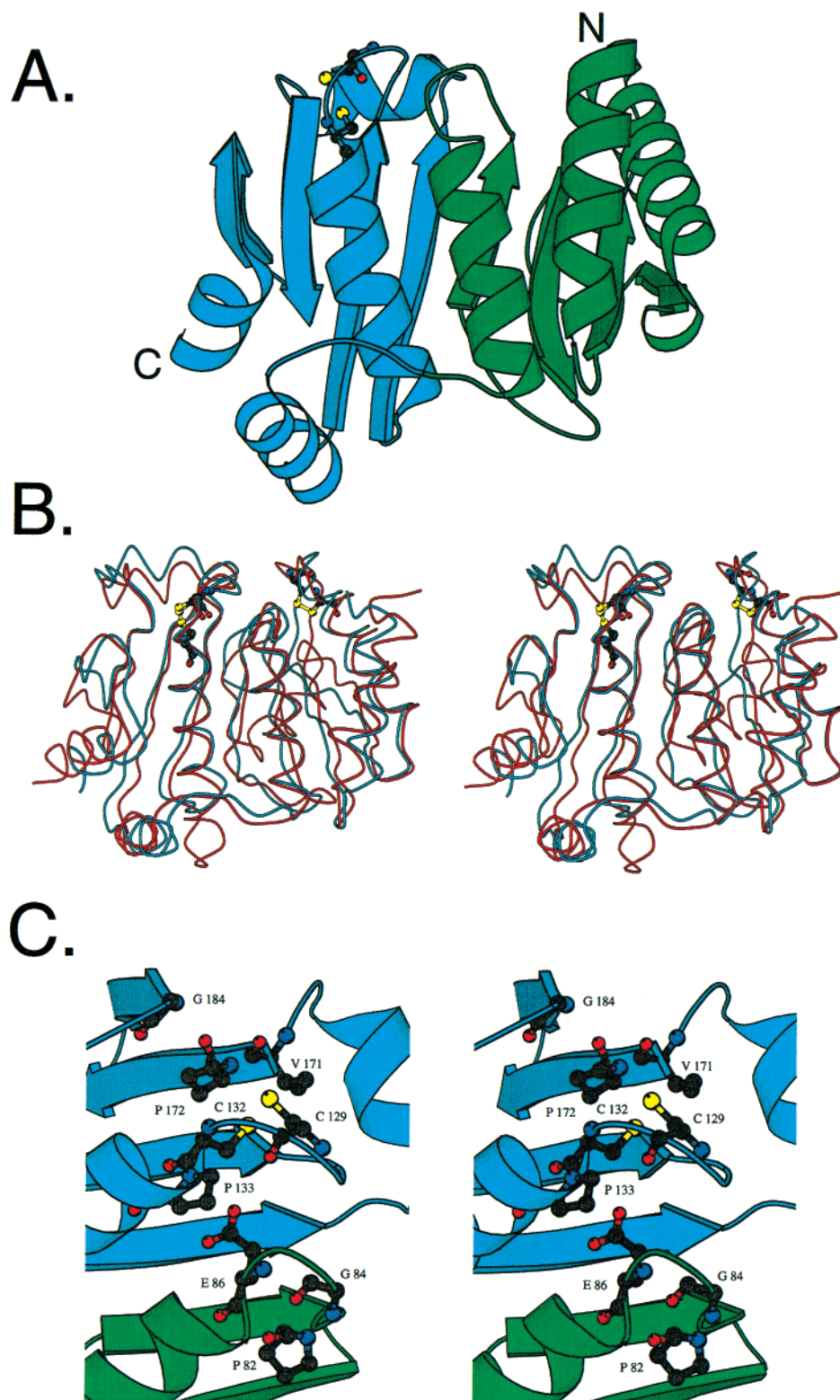


FIGURE 6: Structure of the NTD. (A) Ribbons representation of the NTD (residues 1–195) with separate colors for the two thioredoxin folds (green for the N-terminal half and light blue for the C-terminal half). (B) Stereoview of the NTD (light blue) overlaid with *Pf* PDO (red). The rmsd for the overlay is 1.8 Å for 196 equivalent  $C_{\alpha}$  atoms. The main chain is represented as a coil, and the redox centers for NTD (Cys129–Cys132) and PDO (Cys35–Cys38 and Cys146–Cys149) are inserted. (C) Stereoview of the NTD active site, with thioredoxin folds colored as described for panel A. All nine absolutely conserved residues (Figure 4A) are shown. Cys132  $S_{\gamma}$  is completely solvent inaccessible, while Cys129 is on the surface and exposed. Note that Pro82, Gly84, and Glu86 are all derived from the first thioredoxin fold. This figure was generated using MOLSCRIPT (29).

the NTD connected by a mobile linker to the FAD domain. The fact that the NTD acts as an “appended” substrate during catalysis is supported by the crystal structure. The positions of the two redox centers are more than 33 Å away from

each other, with the NADH/SS redox center near the flavin and the NTD redox center exposed to the solvent (Figure 3). As the NADH/SS domain rotates during catalysis, bringing the TrxR-like dithiols to the surface, the NTD is

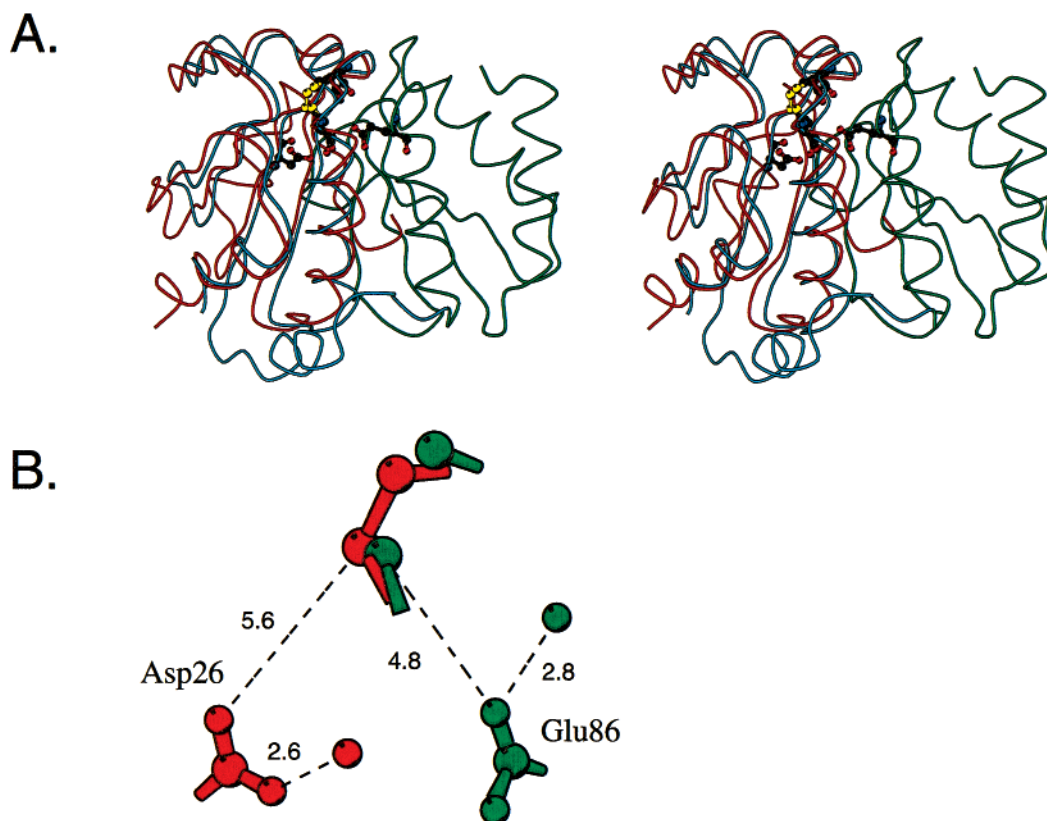


FIGURE 7: Comparisons of the active sites of the NTD and *E. coli* Trx. (A) Stereoview of the C-terminal Trx fold of the NTD (Trx folds 1 and 2 colored green and light blue, respectively) overlaid on the basis of C $\alpha$  atoms with *E. coli* Trx (red), with main chain atoms represented as a coil (rmsd of 2.5 Å for 85 equivalent C $\alpha$  atoms). The redox-active cysteines/cystine for both enzymes are inserted, as well as Glu86 of the NTD and Asp26 of *E. coli* Trx. (B) Closeup view of three overlaid key residues: the disulfide, Asp26, and an interacting water of *E. coli* Trx (red) and the dithiols, Glu86, and an interacting water of the NTD (green). Distances (in angstroms) are depicted by dashed lines. The carboxylates of both acids and all four of the sulfurs of the active sites lie in the same plane, with the carboxylates in similar relative orientations and distances with regard to the interchange thiol, albeit with their positions reflected through an approximate mirror containing the interchange thiol sulfur atom. This figure was generated using MOLSCRIPT (29).

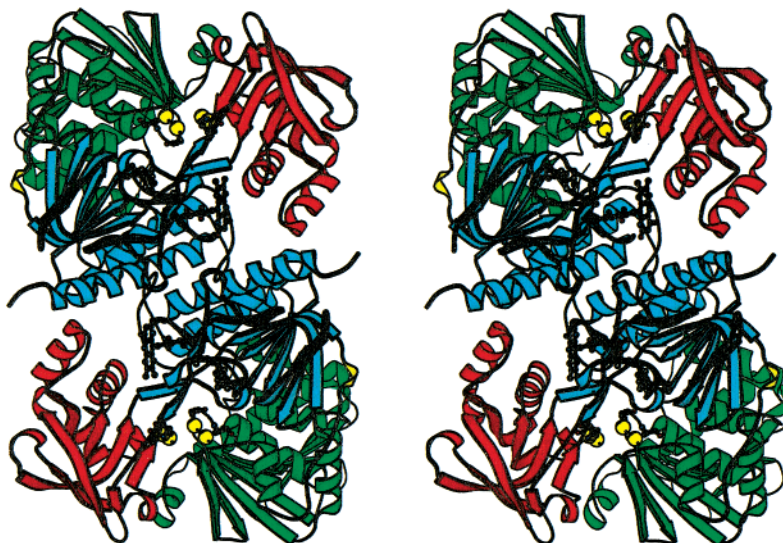


FIGURE 8: Stereoview of the hypothetical alternate conformation of AhpF that would allow for NTD reduction. Domains are colored as described in the legend of Figure 3, and the FAD domains are in the same orientations, to allow easy comparison. There are no steric clashes that would prevent the large-scale motions or final conformation proposed with the exception of a few surface side chains that would require minor adjustments. The two redox-active disulfide centers are adjacent, and the NADH binding site is now near the isoalloxazine ring. To achieve this conformation, a minimal change involves unraveling the first turn of the helix of the flexible linker (yellow). Such an unraveling of the linker helix is supported by limited proteolysis experiments. This figure was generated using MOLSCRIPT (29).

still not in a productive conformation to be reduced with its redox-active disulfide on the opposite face of the molecule. Irrespective of whether electron transfer occurs in an

intramolecular or intermolecular fashion, the NTD will have to move a relatively large distance to reach the NADH/SS dithiols. Using the TrxR–Trx interaction as a template for

modeling the alternate conformation of AhpF, we are able to exclude the intermolecular pathway of NTD reduction (Figure 7). Concurrent with our observations, Reynolds and Poole (40) have confirmed the intramolecular pathway for NTD reduction based on experiments with heterodimers of AhpF mutants, where only mutants capable of intramolecular NTD reduction were active. With regard to the reduction of AhpC, the conformation of AhpF we observe in the crystal may not represent a catalytically relevant intermediate. Although the NTD redox centers are directed toward solvent in the structure, it is possible that in solution the NTD is very mobile and different (or several different) conformations are involved in the binding and reduction of AhpC.

One unfortunate result in our structure is that the TrxR-like disulfide is displaced by a bound chloride, resulting in strained geometry and bad contacts with surrounding atoms (Figures 2B and 5B). Since chloride dramatically influenced crystallization, we hypothesize that the particular orientation of the NADH/SS domain in the crystal is a result of the binding of chloride and stabilization of the flexible NADH/SS domain. Surprisingly, 1 M chloride does not inhibit AhpF activity in solution (data not shown), so it is possible that indirect effects of crystal packing (together with chloride binding) serve to offset the strain in the disulfide. Thus, despite the interesting close approach of Cys348 and the catalytically important Asp349 (34), we have no reason to believe this conformation of the disulfide is mechanistically relevant.

*A New Family of Thioredoxin-like Disulfide Reductases.* In Trx, Asp26 is proposed to maintain the reduced  $pK_a$  of the attacking thiolate (Cys32) and act as a proton sink during acid–base catalysis (36–39). As seen in the overlays (Figure 7A), the conserved Glu86 of NTD is strikingly similar to the conserved Asp26 in *E. coli* Trx in regard to their local, hydrophobic environments and relationship to the redox-active disulfide; both acids lie in the same plane relative to the sulfur atoms and are related by pseudo-mirror symmetry (Figure 7B). A similar mirror symmetry relationship of active sites has been reported in the comparison of the catalytic triads of serine proteases with lipases (41–43). We propose that Glu86 is functionally equivalent to *E. coli* Trx Asp26.

Most striking in the overlay is that Glu86 is in the N-terminal Trx fold, while the redox-active disulfide is in the C-terminal Trx fold (Figure 6C). Ren et al. (12) suggest that the two “fused” thioredoxin folds seen in the PfpDO (and now the NTD) arose from an ancient gene duplication event. We would extend this hypothesis, and suggest that the fusion event was made irreversible by the loss of a Trx-like acid, and the compensatory co-option of a catalytic acid from the first folding unit. Given the observation that the N-terminal disulfide in PfpDO is buried and the lack of a corresponding disulfide in the NTD, it is possible that it serves a purely structural role, and is not catalytically active (Figure 6B). We propose a new class of Trx-like protein disulfide reductases based on this novel active site architecture, of which the NTD is the first example with a known function. We suggest that these be designated peroxiredoxin disulfide reductases.

*Thiol–Thiolate Hydrogen Bonding in the NTD.* The redox center in the NTD is in the reduced (dithiol) state, with a sulfur–sulfur distance of only 3.04 Å (Figure 2A). This is substantially closer than the expected van der Waals radii

(3.60 Å) (44), and is suggestive of a special interaction. Thiol–thiol hydrogen bonding is unlikely, since that involves larger separations; neutron diffraction studies of L-cysteine gave a thiol–thiol hydrogen bond distance of 3.85 Å and  $C_\beta-S_\gamma-S_\gamma$  bond angles of 96° and 70° for the donor and acceptor, respectively (45), and a 1.7 Å resolution structure of reduced human thioredoxin reported a thiol–thiol hydrogen bond distance of 3.9 Å and  $C_\beta-S_\gamma-S_\gamma$  bond angles of 105° and 70° for the donor and acceptor, respectively (46). In the latter study, crystals were at pH 3.8, which is much below the  $pK_a$  of 6.3 of the attacking thiolate (47), so that both sulfurs were definitely present as thiols.

We suggest the close interaction we observe is a stronger thiol–thiolate hydrogen bond. Although thiol–thiolate hydrogen bonding has not been observed in small molecule crystal structures, it has been proposed to exist in Trx-related proteins as a means of stabilizing the attacking thiolate (48). Recent NMR studies have confirmed the thiol–thiolate hydrogen bond of reduced glutaredoxin, a member of the Trx family (49). Crystallographic evidence for thiol–thiolate hydrogen bonding comes from the 2.7 Å resolution structure of reduced DsbA, where thiol–thiolate distances of 3.4 and 3.5 Å were reported (50). Recently, Lennon et al. reported a short sulfur–sulfur distance of 3.09 Å in the 2.5 Å resolution crystal structure of reduced TrxR, and suggested this represents a thiol–thiolate hydrogen bond (51). This is very similar to the 3.04 Å separation we see in our higher-resolution structure. The  $C_\beta-S_\gamma-S_\gamma$  angles of 109° and 83° for Cys132 and Cys129, respectively, implicate Cys132 as the donor and Cys129 as the acceptor, consistent with Cys129 being the attacking thiolate. Although the  $pK_a$  of Cys129 is not known, we expect it to be less than 5, since the crystals are at pH 5.6. In addition, we are able to predict that the redox potential of the NTD redox-active disulfide will be higher than that in the NADH/SS domain (at least at this pH). The fortuitous presence of a stable thiol–thiolate hydrogen bond in the NTD provides an opportunity to probe the factors contributing to the stabilization of the attacking thiolate in Trx-like proteins.

## ACKNOWLEDGMENT

Thanks to the staff at CHESS and ALS for their support and guidance. We also thank Savvas Savvides and Rick Faber for many helpful discussions in bringing this project to fruition.

## NOTE ADDED IN PROOF

B. Bieger and L.-O. Essen have determined the structure of the TrxR-like portion of AhpF (in press in *Journal of Molecular Biology*). Their structure reveals the NADH/SS redox-active disulfide in a conformation similar to that seen in *E. coli* TrxR.

## REFERENCES

- Jacobson, F. S., Morgan, R. W., Christman, M. F., and Ames, B. N. (1989) *J. Biol. Chem.* 264, 1488–1496.
- Christman, M. F., Morgan, R. W., Jacobson, F. S., and Ames, B. N. (1985) *Cell* 41, 753–762.
- Morgan, R. W., Christman, M. F., Jacobson, F. S., Storz, G., and Ames, B. N. (1986) *Proc. Natl. Acad. Sci. U.S.A.* 83, 8059–8063.

4. Poole, L. B., and Ellis, H. R. (1996) *Biochemistry* 35, 56–64.
5. Niimura, Y., Poole, L. B., and Massey, V. (1995) *J. Biol. Chem.* 270, 25645–25650.
6. Rhee, S. G., Kang, S. W., Netto, L. E., Seo, M. S., and Stadtman, E. R. (1999) *Biofactors* 10, 207–209.
7. Chae, H. Z., Robison, K., Poole, L. B., Church, G., Storz, G., and Rhee, S. G. (1994) *Proc. Natl. Acad. Sci. U.S.A.* 91, 7017–7021.
8. Poole, L. B. (1996) *Biochemistry* 35, 65–75.
9. Poole, L. B., Reynolds, C. M., Wood, Z. A., Karplus, P. A., Ellis, H. R., and Li Calzi, M. (2000) *Eur. J. Biochem.* 267, 6126–6133.
10. Tartaglia, L. A., Storz, G., Brodsky, M. H., Lai, A., and Ames, B. N. (1990) *J. Biol. Chem.* 265, 10535–10540.
11. Poole, L. B., Godzik, A., Nayeem, A., and Schmitt, J. D. (2000) *Biochemistry* 39, 6602–6615.
12. Ren, B., Tibbelin, G., de Pascale, D., Rossi, M., Bartolucci, S., and Ladenstein, R. (1998) *Nat. Struct. Biol.* 5, 602–611.
13. Waksman, G., Krishna, T. S., Williams, C. H., Jr., and Kuriyan, J. (1994) *J. Mol. Biol.* 236, 800–816.
14. Lennon, B. W., Williams, C. H., Jr., and Ludwig, M. L. (2000) *Science* 289, 1190–1194.
15. Reynolds, C. M., and Poole, L. B. (2000) *Biochemistry* 39, 8859–8869.
16. Li Calzi, M., and Poole, L. B. (1997) *Biochemistry* 36, 13357–13364.
17. Ramakrishnan, V., Finch, J. T., Graziano, V., Lee, P. L., and Sweet, R. M. (1993) *Nature* 362, 219–223.
18. Jancarik, J., and Kim, S. H. (1991) *J. Appl. Crystallogr.* A43, 1–5.
19. Rodgers, D. W. (1997) *Methods Enzymol.* 276, 183–203.
20. Collaborative Computational Project, No. 4 (1994) *Acta Crystallogr. D50*, 760–763.
21. Otwinowski, Z., and Minor, W. (1996) *Methods Enzymol.* 276, 307–326.
22. Diederichs, K., and Karplus, P. A. (1997) *Nat. Struct. Biol.* 4, 269–275.
23. Brunger, A. T., Adams, P. D., Clore, G. M., DeLano, W. L., Gros, P., Grosse-Kunstleve, R. W., Jiang, J. S., Kuszinski, J., Nigles, M., Pannu, N. S., Read, R. J., Rice, L. M., Simonson, T., and Warren, G. L. (1998) *Acta Crystallogr. D54*, 905–921.
24. Sack, J. S., and Quijoch, F. A. (1997) *Methods Enzymol.* 277, 158–173.
25. Abrahams, J. P., and Leslie, A. G. W. (1996) *Acta Crystallogr. D52*, 30–42.
26. Smith, R. F., and Smith, T. F. (1990) *Proc. Natl. Acad. Sci. U.S.A.* 87, 118–122.
27. Smith, R. F., and Smith, T. F. (1992) *Protein Eng.* 5, 35–41.
28. Holm, L., and Sander, C. (1993) *J. Mol. Biol.* 233, 123–138.
29. Kraulis, P. (1991) *J. Appl. Crystallogr.* 24, 946–950.
30. Hanukoglu, I., and Gutfinger, T. (1989) *Eur. J. Biochem.* 180, 479–484.
31. Wierenga, R. K., Terpstra, P., and Hol, W. G. (1986) *J. Mol. Biol.* 187, 101–107.
32. Scrutton, N. S., Berry, A., and Perham, R. N. (1990) *Nature* 343, 38–43.
33. Ponder, J. W., and Richards, F. M. (1987) *J. Mol. Biol.* 193, 775–791.
34. Mulrooney, S. B., and Williams, C. H., Jr. (1994) *Biochemistry* 33, 3148–3154.
35. Altschul, S. F., Gish, W., Miller, W., Myers, E. W., and Lipman, D. J. (1990) *J. Mol. Biol.* 215, 403–410.
36. LeMaster, D. M. (1996) *Biochemistry* 35, 14876–14881.
37. LeMaster, D. M., Springer, P. A., and Unkefer, C. J. (1997) *J. Biol. Chem.* 272, 29998–30001.
38. Dyson, H. J., Jeng, M. F., Tennant, L. L., Slaby, I., Lindell, M., Cui, D. S., Kuprin, S., and Holmgren, A. (1997) *Biochemistry* 36, 2622–2636.
39. Chivers, P. T., and Raines, R. T. (1997) *Biochemistry* 36, 15810–15816.
40. Reynolds, C. M., and Poole, L. B. (2001) *Biochemistry* 40, 3912–3919.
41. Brady, L., Brzozowski, A. M., Derewenda, Z. S., Dodson, E., Dodson, G., Tolley, S., Turkenburg, J. P., Christiansen, L., Huge-Jensen, B., Norskov, L., et al. (1990) *Nature* 343, 767–770.
42. Winkler, F. K., D'Arcy, A., and Hunziker, W. (1990) *Nature* 343, 771–774.
43. Sussman, J. L., Harel, M., Frolow, F., Oefner, C., Goldman, A., Toker, L., and Silman, I. (1991) *Science* 253, 872–879.
44. Bondi, A. (1964) *J. Phys. Chem.* 68, 441–451.
45. Kerr, K. A., and Abrahams, J. P. (1975) *Acta Crystallogr. B31*, 2022–2026.
46. Weichsel, A., Gasdaska, J. R., Powis, G., and Montfort, W. R. (1996) *Structure* 4, 735–751.
47. Forman-Kay, J. D., Clore, G. M., and Gronenborn, A. M. (1992) *Biochemistry* 31, 3442–3452.
48. Jeng, M. F., Holmgren, A., and Dyson, H. J. (1995) *Biochemistry* 34, 10101–10105.
49. Nordstrand, K., Aslund, F., Meunier, S., Holmgren, A., Otting, G., and Berndt, K. D. (1999) *FEBS Lett.* 449, 196–200.
50. Guddat, L. W., Bardwell, J. C., and Martin, J. L. (1998) *Structure* 6, 757–767.
51. Lennon, B. W., Williams, C. H., Jr., and Ludwig, M. L. (1999) *Protein Sci.* 8, 2366–2379.

BI002765P